Broadband noise prediction of stochastic sources based on the linearized Euler equations

César Legendre[a] , Athanasios Poulos, Benjamin de Brye, Alexis Talbot, Maxime Raskin & Yves Detandt
Free Field Technologies S.A., Axis Park Louvain-La-Neuve, Rue Emile Francqui 9, B-1435 Mont-Saint-Guibert, Belgium.

ABSTRACT

Hybrid computational methods for aeroacoustics rely on the correct estimation of the flow solution to properly determine the equivalent noise sources. This flow solution may be obtained using unsteady CFD simulations that, in most cases, are prohibitive for industrial applications due to the large computational cost required. The hybrid approach for computational aeroacoustics presented in this work is based on SNGR method (Stochastic Noise Generation and Radiation) for synthetizing noise sources to be applied in the right-hand side of the Linearized Euler Equations (LEE). The stochastic method for generating the aeroacoustic sources depend on the time averaged solution of the flow field (RANS), reducing the computational cost associated to the CFD simulation. On the other hand, the acoustic propagation is solved by means of a high-order adaptive Discontinuous Galerkin (DG) scheme in time domain. This scheme is chosen due to its ability to accurately represent the phenomena involved and its high parallel scalability allowing the analysis of large/high frequency problems at acceptable computational costs from an industrial perspective. Subsequently, the hybrid method proposed is applied to a full-size car using RANS-based results for the source synthetization and GPU acceleration for the computation of the broadband acoustic field. Finally, the influence of the car's speed on the noise generation is assessed.

1 INTRODUCTION

Direct methods for estimating aerodynamic noise in industrial applications are prohibitive due to the large computational cost required. Because of the disparity of characteristic lengths between fluid dynamics and acoustics,[1,2] hybrid computational methods should be employed to overcome this problem. Although hybrid computational methods are much less expensive in terms of human and computational resources than direct methods for aeroacoustics, the former still require accurate unsteady CFD solutions, usually **L**arge **E**ddy **S**imulation (LES) CFD, to properly estimate the equivalent noise sources. Such LES-CFD solutions are frequently incompatible with industrial time scales, in which a maximum number designs or prototypes must be evaluated in the shortest time possible.[3] In contrast, **R**eynolds-**A**veraged **N**avier-Stokes (RANS) solutions represent an appropriate trade-off because they are much less computationally expensive than LES-CFD methods while still providing correct estimations of the time-averaged aerodynamic fields.

---

[a]email: cesar.legendre@fft.be

In the light of above, the SNGR (**S**tochastic **N**oise **G**eneration and **R**adiation) approach allows the reconstruction of the turbulent velocity fluctuations based on the RANS-CFD mean flow for determining the equivalent noise sources. The stochastic method synthesizes the turbulent velocity field from a finite sum of statically independent Fourier modes which amplitudes are function of the turbulent kinetic energy and dissipation rate estimated previously in the RANS-CFD simulation.[2]

The present article describes an efficient implementation of the LEE (**L**inearized **E**uler **E**quations) using a high-order adaptive DG scheme in time domain[4] in *ActranDGM* solver, with aeroacoustic sources imposed on the right-hand side of the momentum equation[5,6] (Section §2). The sources are determined from turbulent velocity fluctuations synthesized using SNGR approach (section §2.2), while *ActranDGM* is used as the acoustic solver. Since the DG method operates with large-size elements of high $p-$order interpolation, the aerodynamic sources are sub-sampled at the Gauss' points inside the element to take into account the small turbulent scales present in comparison to the wavelength of the problem. Due to the large size of the problem and number of configurations computed, the numerical results obtained are compared in relative terms with empirical scaling laws based on experimental[7,8] and simulation data.[7] The advantages that represent the implementation of an hybrid approach in time domain for aeroacoustics (LEE with sources) in a DG context are the following: (i) the p-adaptivity allows to use the same mesh for different frequencies adjusting dynamically the elements' order; and (ii) high parallel scalability suited to large acoustic problems and high frequency, characteristic of industrial problems. Furthermore, the case selected is a realistic hatchback vehicle at seven velocity regimes from 80 km/h to 200 km/h as depicted in figures 1a-d. The main objective is to observe how the overall noise produced by the turbulent structures around the vehicle scales with respect to the vehicle's velocity. The paper is organized as follows, the formulation of the SNGR method for the generation of sources and the LEE DG-solver for the acoustic propagation are presented in section §2. Then, the flow solution based on RANS-CFD computation (section §3) and the acoustic model (section §4) are described. Finally, the results are discussed and analysed (section §5) followed by some concluding remarks and possible further investigations (section §6).

2 THEORETICAL BACKGROUND

The linearised Euler equations with source terms at the right-hand side may be written in compact form as follows:

$$\frac{\partial \boldsymbol{q}}{\partial t} + \frac{\partial}{\partial x_j}\left(\mathbb{F}_j.\boldsymbol{q}\right) - \boldsymbol{s}.\boldsymbol{q} = \mathbb{R}, \tag{1}$$

in which the vector of variables $\boldsymbol{q} = [\rho, u, v, w, p]$ contains the fluctuating density, velocity and pressure. The flux matrix $\mathbb{F}_j$, the gradient matrix $\boldsymbol{s}$ and the vector of sources $\mathbb{R}$ are expressed as:

$$\mathbb{R} = \begin{bmatrix} 0 \\ \left(R_1 - \bar{R}_1\right)/\rho_0 \\ \left(R_2 - \bar{R}_2\right)/\rho_0 \\ \left(R_3 - \bar{R}_3\right)/\rho_0 \\ 0 \end{bmatrix}, \quad \mathbb{F}_j = \begin{bmatrix} v_j^0 & \rho_0\delta_{1j} & \rho_0\delta_{2j} & \rho_0\delta_{3j} & 0 \\ 0 & v_j^0 & 0 & 0 & \delta_{1j}/\rho_0 \\ 0 & 0 & v_j^0 & 0 & \delta_{2j}/\rho_0 \\ 0 & 0 & 0 & v_j^0 & \delta_{3j}/\rho_0 \\ 0 & \rho_0 c^2\delta_{1j} & \rho_0 c^2\delta_{2j} & \rho_0 c^2\delta_{3j} & v_j^0 \end{bmatrix}, \tag{2a,b}$$

$$
s = \begin{bmatrix}
0 & 0 & 0 & 0 & 0 \\[4pt]
\dfrac{1}{\rho_0^2}\dfrac{\partial p_0}{\partial x} & \dfrac{\partial v_j^0}{\partial x_j} - \dfrac{\partial u_0}{\partial x} & -\dfrac{\partial u_0}{\partial y} & -\dfrac{\partial u_0}{\partial z} & -\dfrac{1}{\rho_0^2}\dfrac{\partial \rho_0}{\partial x} \\[10pt]
\dfrac{1}{\rho_0^2}\dfrac{\partial p_0}{\partial y} & -\dfrac{\partial v_0}{\partial x} & \dfrac{\partial v_j^0}{\partial x_j} - \dfrac{\partial v_0}{\partial y} & -\dfrac{\partial v_0}{\partial z} & -\dfrac{1}{\rho_0^2}\dfrac{\partial \rho_0}{\partial y} \\[10pt]
\dfrac{1}{\rho_0^2}\dfrac{\partial p_0}{\partial z} & -\dfrac{\partial w_0}{\partial x} & -\dfrac{\partial w_0}{\partial y} & \dfrac{\partial v_j^0}{\partial x_j} - \dfrac{\partial w_0}{\partial z} & -\dfrac{1}{\rho_0^2}\dfrac{\partial \rho_0}{\partial z} \\[10pt]
0 & \rho_0 \dfrac{\partial c^2}{\partial x} & \rho_0 \dfrac{\partial c^2}{\partial y} & \rho_0 \dfrac{\partial c^2}{\partial z} & \dfrac{c^2}{\rho_0}v_j^0\dfrac{\partial \rho_0}{\partial x_j} + \dfrac{\partial v_j^0}{\partial x_j}
\end{bmatrix},
\tag{3}
$$

where the aerodynamic source R applied to the momentum equation is defined by:

$$
R_j = -\frac{\partial \rho u_i^t u_j^t}{\partial x_i}, \quad \overline{R}_j = -\frac{\overline{\partial \rho u_i^t u_j^t}}{\partial x_i}.
\tag{4a,b}
$$

in which u_i^t is the turbulent velocity field syntetized using the method described in section §2.2. The "0" index denotes mean flow, either sub-index in the case of mean pressure p_0 and density ρ_0 or super-index for mean velocity v_j^0. The speed of sound is denoted by c while δ_{ij} is Kronecker's delta. Furthermore, the expression of the aerodynamic sources (2a;4a,b) is found by analogy with Lighthill's equation[9,10] in absence of mean flow convection.[2,5]

2.1 Discontinuous Galerkin method

In addition, by multiplying equation (1) by a Lagrange high-order polynomial shape function $\mathbf{N}_\alpha$ and integrated over the volume Ω follows:[5]

$$
\int_\Omega \mathbf{N}_\alpha \frac{\partial \boldsymbol{q}}{\partial t} d\Omega + \int_\Omega \mathbf{N}_\alpha \frac{\partial}{\partial x_j}\left(\mathbb{F}_j . \boldsymbol{q}\right) d\Omega - \int_\Omega \mathbf{N}_\alpha \boldsymbol{s}.\boldsymbol{q} d\Omega = \int_\Omega \mathbf{N}_\alpha \mathbb{R} d\Omega.
\tag{5}
$$

Integrating by parts the second term of equation (5) to transfer the derivative in space $\partial/\partial x_j$ to the shape functions $\mathbf{N}_\alpha$, equation (5) results in:

$$
\int_\Omega \mathbf{N}_\alpha \frac{\partial \boldsymbol{q}}{\partial t} d\Omega = \int_\Omega \frac{\partial \mathbf{N}_\alpha}{\partial x_j}\mathbb{F}_j . \boldsymbol{q} d\Omega + \int_\Omega \mathbf{N}_\alpha \boldsymbol{s}.\boldsymbol{q} d\Omega - \oint_\Gamma \mathbf{N}_\alpha (\mathbb{F}_j.\boldsymbol{q}).\boldsymbol{n} d\Gamma + \int_\Omega \mathbf{N}_\alpha \mathbb{R} d\Omega
\tag{6}
$$

the variational formulation used in the discontinuous Galerkin (DG) method. DG methods are characterized by discontinuous solutions from one element to another in which the surface integral of equation (6) or flux is computed from the solutions on both sides of the element. An advantage of this variational formulation (6) is that using an explicit time discretization, the linear system becomes block diagonal, and the matrix inversions at each time step can be replaced by matrix multiplications. Finally, the last term of equation (6) represents the volume sources applied to the momentum equation. Since the acoustics and aerodynamic sources are very disparate in terms of characteristic length, the variability of the source terms is taken into account inside element by the high-order Lagrange shape functions $\mathbf{N}_\alpha$ of the numerical algorithm.

2.2 SNGR: Synthetization of the turbulent velocity field

In this work, the stochastic noise method is based on a Fourier modes representation of turbulent velocity fluctuations known as SNGR.[2,11,12] The fluctuating turbulent velocity $\mathbf{u}_t$ is expressed as a

finite sum of N statistically independent random modes as follows (7a):

$$\mathbf{u}_t(\mathbf{x}, t) = 2 \sum_{n=1}^{N} \tilde{u}_n \cos\left(\boldsymbol{k}_n \cdot (\mathbf{x} - \mathbf{u}_0 t) - \omega_n t + \varphi_n\right) \boldsymbol{\sigma}_n, \quad \bar{k} = \sum_{n}^{N} \tilde{u}_n^2, \qquad \text{(7a,b)}$$

where $\boldsymbol{k}_n$ is the wavenumber and $\bar{k}$ is the turbulent kinetic energy (7b) or TKE. The turbulent ve-
locity amplitude $\tilde{u}_n = \sqrt{E(k)\Delta k}$ of the nth mode depends on the turbulent kinetic energy spectrum
$E(k)$. In addition, $\mathbf{u}_0$ is the mean local velocity obtained from the RANS-CFD simulation and ω_n,
φ_n and $\boldsymbol{\sigma}_n$ are the angular velocity and statistically random phase angle and orientation vector of
the nth Fourier mode respectively. The direction ς_n of the wavenumber $\boldsymbol{k}_n$, i.e. $\boldsymbol{k}_n =\mid \boldsymbol{k}_n \mid \varsigma_n$, is
also chosen randomly. Because each Fourier mode is assumed incompressible $\boldsymbol{\kappa}_n \cdot \boldsymbol{\sigma}_n = 0$ holds[11]
stating that the turbulent velocity $\mathbf{u}_t$ is always perpendicular to the wavenumber $\boldsymbol{k}_n$. Furthermore,
the turbulent kinetic energy spectrum $E(k)$ is chosen from experience or from knowledge of the
simulated case. In the present work, the Von Kármán-Pao spectrum (8a) is used:

$$E(k) = A\frac{2}{3}\frac{\bar{k}}{k_e}\frac{(k/k_e)^4}{[1 + (k/k_e)^2]^{17/6}}\exp\left(-\frac{2k}{k_\nu}\right), \ \bar{k} = \int_0^\infty E(k)dk, \ \varepsilon = 2\nu\int_0^\infty k^2 E(k)dk. \ \text{(8a-c)}$$

where $k_\nu = (\varepsilon/\nu^3)^{(1/4)}$ is the Kolmorogov's wavenumber depending on the molecular viscosity
ν and turbulent dissipation rate ε. The wavenumber associated with the most energetic eddies is
denoted as k_e and corresponds to the maximum of the spectrum $E(k)$ and A is a scaling factor
that must satisfy the conditions (8c,d). Additionally, the macroscopic turbulence parameters such
as: (i) mean flow fields; (ii) turbulent kinetic energy $\bar{k}$; and (iii) turbulent dissipation rate ε are
estimated using a RANS-CFD simulation as a first step. Secondly, a finite number of Fourier
modes are generated to represent the turbulent velocity field from such macroscopic parameters.
Finally, since turbulence is not a deterministic process, several realizations of the turbulent velocity
field are generated for computing the aerodynamic sources.

3   FLOW SOLUTION AND SOURCE GENERATION

The steady CFD simulation is performed using Cradle *SCTetra*.[13] The vehicle used is a generic
hatchback vehicle and the model includes the external surfaces as well as internal components
inside the engine bay. The surrounding domain has dimensions $50 \times 60 \times 40$ m while the car has a
length of $L = 4.33$ m. The side and top patches of the model domain are modeled as slip boundary
conditions while the ground is modeled as moving, see figure 1b. Constant velocity is considered
for the inlet boundary condition while the static pressure is fixed at the outlet. The velocity at the
inlet ranges from 80 km/h to 200 km/h with a step of 20 km/h for a total of seven different CFD
simulations, for instance the velocity contours for the middle value of inlet velocity 140 km/h are
depicted in figure 1c-d . The flow is incompressible and air at standard conditions has been used as
a fluid with constant density $\rho_0 = 1.206$ kg/m^3 and kinematic viscosity $\nu = 1.83 \times 10^{-5}$ m^2/s.

The mesh is an unstructured tetrahedral mesh consisting of around 25 million cells with pris-
matic elements used for the boundary layer definition. Various box refinements are used around the
vehicle which allow to capture appropriately the turbulent kinetic energy. The turbulent model used
is the High-Reynolds Kato-Launder $\bar{k}$-ε model[14] with the modified production term for controlling
the overproduction of the turbulent kinetic energy in areas of strong accelerations. The average y+
is around 50. The simulations were performed on a cluster of 48 Intel(R) Xeon(R) CPU Gold 6148
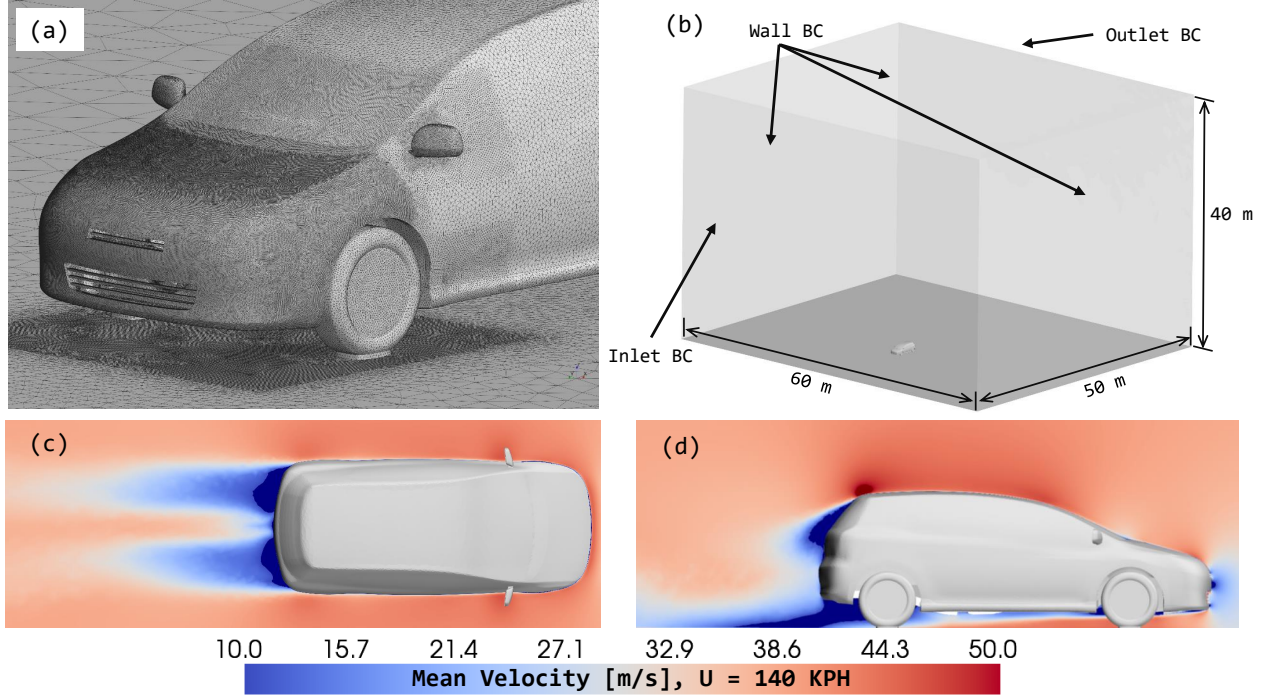@ 2.40 GHz processors with the computation cost being at 72 CPU.h per simulation.

Fig. 1. – CFD model. (a) Detail of mesh used in the CFD simulation close to side mirror. Note that the mesh is finer in the vicinity of the mirror. (b) CFD model with dimensions indicated over the figure. (c) Top view of mean velocity around the vehicle for inlet velocity of 140 km/h. (d) same as (c) but in side-view.
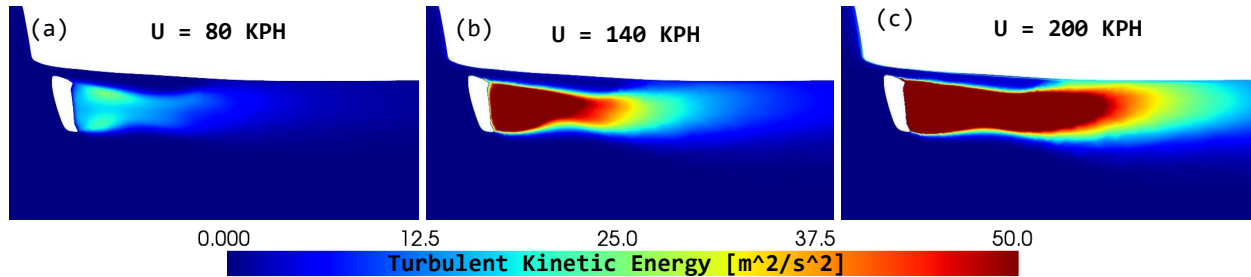

Fig. 2. – Turbulent kinetic energy contour around the side mirror for three values of inlet velocity 80 km/h, 140 km/h and 200 km/h .

In order to properly identify the noise sources using the SNGR method, the turbulent kinetic energy field needs to be sufficiently smooth. The source generation is based on 30 Fourier modes to represent the turbulent velocity field using Von Kármán-Pao's turbulent spectrum over five realizations. To improve memory and CPU usage, the synthetization of the turbulent velocity field is reduced to the CFD cells with the most energetic contribution, this selection is based arbitrarily chosen threshold level. Figures 2a-c show the turbulent kinetic energy field in the area close to the side mirror for an inlet velocity of (i) 80 km/h, (ii) 140 km/h and (iii) 200 km/h. As the CFD simulation, the computation of sources were performed in the same computer architecture using 4 Intel(R) Xeon(R) CPU Gold 6148 @ 2.40 GHz processors with a memory consumption of 30 GB at each processor, the computational cost per case rise up 21.4 CPU.h with a memory storage needed of 28 Gb per case.

4 ACOUSTIC MODEL

The acoustic propagation of aerodynamic sources synthesized using SNGR method based on the aerodynamic flow solution around a hatchback's vehicle is considered here. The vehicle is immersed in a fluid at rest placed in a semi-anechoic room. As a consequence, the the aerodynamic noise produced by the turbulence generated around the vehicle is the only acoustic source. The fluid media for the propagation of the acoustic waves is assumed homogeneous at rest with constant mass density (same as in the CFD model) and speed of sound $c_0 = 340 \text{ m/s}$. Even for the highest velocity $U = 200 \text{ km/h}$ (55.5 m/s), the Mach number $M = 0.16$ is sufficiently small to neglect convection effects. The acoustic model relies on a time scheme model solved by means of *ActranDGM* solver, this model solves the LEE with source terms in the momentum equation (section §2) using DG methods with $p-$adaptivity for the interpolation order inside the element.
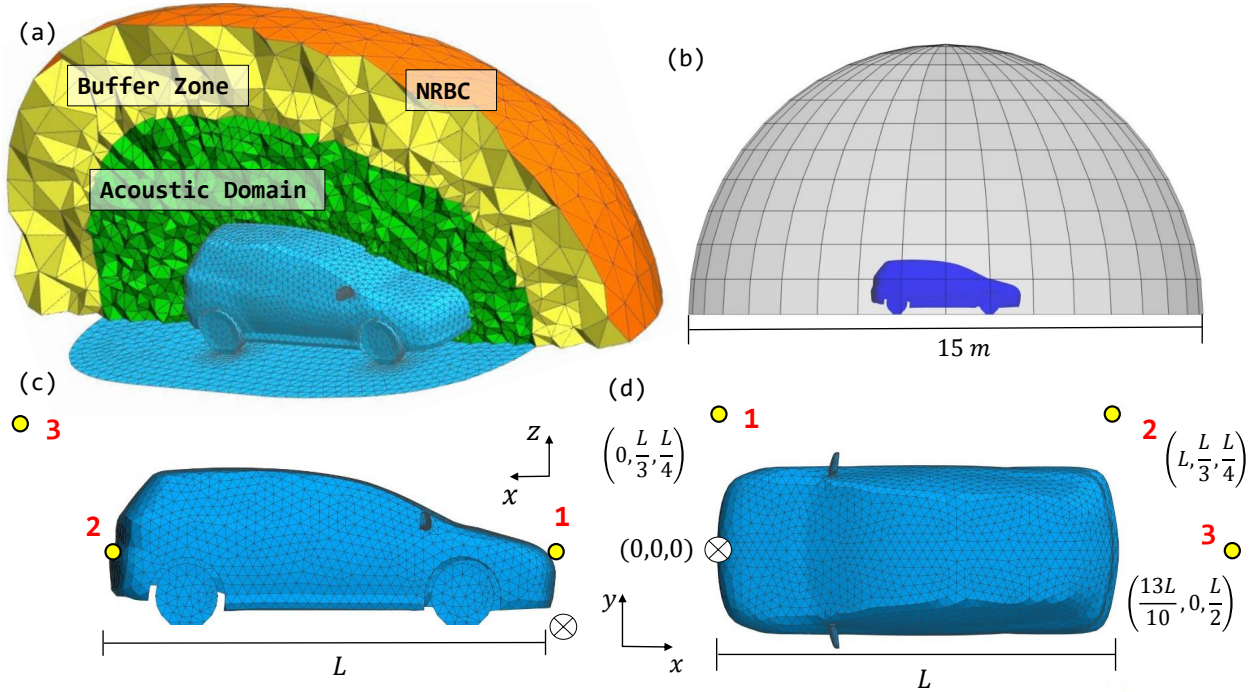

Fig. 3. – Acoustic model. (a) Mesh used in the acoustic model. (b) Semi-spherical surface of 15 m of diameter centered at the vehicle's centroid used to compute the sound power and averaged pressure. (c) Position of the three virtual microphones placed in the near field depicted as yellow circles (side-view) with respect to the center placed at $(0, 0, 0)$ m depicted with the symbol $\otimes$; (d) Similar as (c) but top-view in which the position of each virtual microphones is indicated at the figure in terms of the vehicle's length L.

The mesh used consists in (figure 3a): (i) an acoustic domain corresponding to the air volume surrounding the vehicle (green domain, figure 3a); (ii) a source domain where the acoustic sources are imposed coinciding with the previous acoustic domain (green domain, figure 3a); (iii) a buffer zone to damp the sound waves propagated out the physical domain (yellow domain, figure 3a); and (iv) a non-reflecting boundary condition surrounding the buffer zone (orange 2D-domain, figure 3a). All the domains necessary for the above model form a mesh of 112906 3D-Tetrahedra with 1002 2D-Triangular elements. Since the DG method is based on $p-$adaptivity, the mesh size is designed to have an interpolation ranging from 6 to 10 to assure good quality in the solution for

frequencies up to 3 KHz. The degrees of freedom for the *ActranDGM* model rise up to $N_{\text{dof}} = 1.43 \times 10^8$ ($2.88 \times 10^7 \times 5$ realizations) for the maximal frequency. Finally, it is reasonable to think that the computed sources are less reliable when the CFD mesh coarsens. Therefore, a spatial filter has been used to mitigate the truncation effects at the end of the zone where the CFD results are converted into sources. A relative independence of the position of this filter has been observed in additional investigations performed (not presented here).
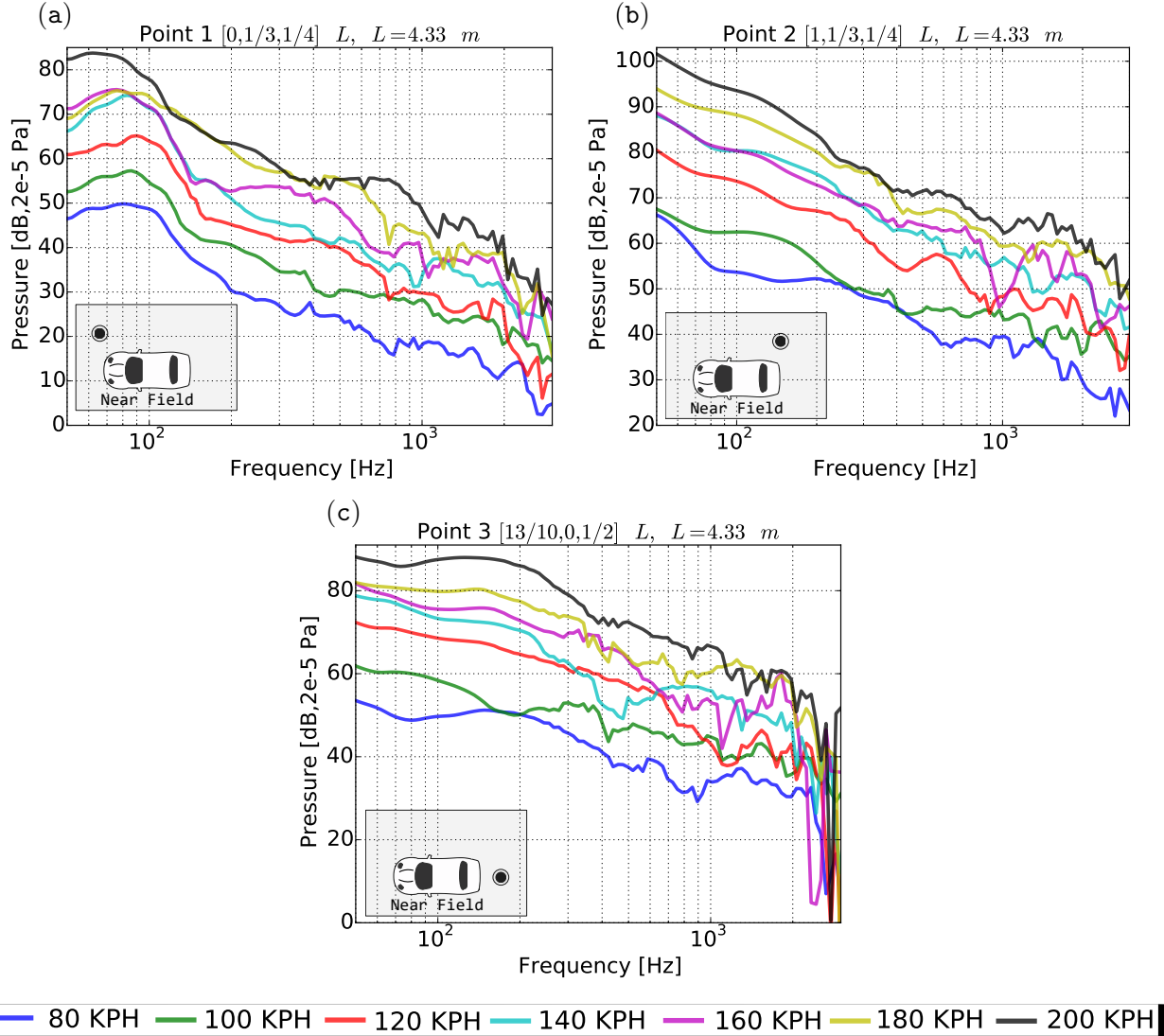

Fig. 4. – *Acoustic pressure spectrum for the three virtual microphones in dB ($p_{ref} = 2 \times 10^{-5}$Pa) placed in the near field. The position of each microphone is indicated at the figure and it is expressed in terms of the car's length L.*

5   RESULTS

Broadband computations are performed for the seven velocity configurations (80 km/h to 200 km/h) at 100 frequencies from 50 Hz to 3000 Hz using a logarithmic frequency step. The velocity

values of the vehicle were chosen as in Hartmann et al.[7] Albeit, the present configuration differs as that presented in Hartmann et al.,[7] similar scaling laws for the overall noise production are expected. Therefore, the main objective is to observe how the overall noise produced by the turbulent structures around the vehicle scales with respect to the vehicle's velocity. Three types of noise indicators are computed. First, the near field pressure is computed in three different positions relatively far from the turbulent wake (side mirror and vehicle's rear wakes) and expressed in terms of the vehicle's length L as depicted in figures 3c,d: (i) Point 1 in the front-right of the vehicle at $(0, L/3, L/4)$; (ii) Point 2 in the rear-right of the vehicle at $(L, L/3, L/4)$; and (iii) Point 3 at the rear-top of the vehicle far from the main wake at $(13L/10, 0, L/2)$. Secondly, the root average square pressure in dB ($p_{ref} = 2 \times 10^{-5}$Pa) is computed from a collection of 3500 virtual microphones in the far field evenly spaced in a semi-sphere of 15 m of diameter centered at the vehicle's centroid as depicted in figure 3b. Finally, the sound power was also computed (dB, $W_{ref} = 1 \times 10^{-12}$ W) in the same semi-spherical surface surrounding the vehicle (figure 3b) as the surface integral of the acoustic intensity $\mathbf{I} = \frac{1}{2} p \mathbf{v}^*$.

In figures 4a-c, the influence of the vehicle's velocity over the acoustic pressure computed in the three near field virtual microphones may be observed. In the right-front microphone with respect to the vehicle (Point 1, figure 4a) a main lobe is observed for all cases 80 km/h - 200 km/h at low frequencies < 100 Hz. The overall noise perceived for all cases in the whole frequency range 50-3000 Hz is proportional to the vehicle's velocity, in general the noise is increased ~10 dB each 20 km/h from 80km/h to 200km/h. Furthermore, the acoustic spectrum computed at the right-rear of the vehicle (Point 2, figure 4b) generally predicts noise ~18 dB higher for all curves with respect to Point 1 (figure 4a), this is mainly due to the noise produced by the side-mirror and rear wakes that propagates predominantly downstream with flow direction. Also, the tendency for the acoustic pressure predicted in Point 2 (figure 4b) is similar as Point 1 (figure 4a), i.e. an overall pressure increment of ~10 dB each 20 km/h for all velocity configurations. Additionally, the pressure spectrum for the seven vehicle's velocities computed at the rear-top of the vehicle, i.e. Point 3, is presented in figure 4c. In general, the pressure spectra in Point 3 behaves similarly as in Point 1 and Point 2 except for high oscillating amplitudes at high frequencies (> 2000 Hz). The acoustic pressure spectra presented in figures 4a-c represent the local acoustic pressure computed at certain positions. In such positions, zones of silence of high pressure zones may appear depending on the frequency and aerodynamic source configuration. This may explain why some of the curves corresponding to lower vehicle's speed are noisier at particular frequencies than others with higher velocity configurations. For instance, this is the case for 140 km/h (cyan) and 160 km/h (magenta) curves in figure 4b at low-middle frequencies around ~200Hz or also the case for 160 km/h (magenta) and 180 km/h (yellow) curves in figure 4a at low frequencies around ~50Hz. Despite all of this, the trend of ~10 dB increment each 20 km/h is generally present.

In order to overcome some local particular behaviors such as the occurrence of zones of silence or high pressure zones at certain vehicle's velocities or frequency regimes, global indicators are computed based on the far field solution. In figure 5a, the root average square pressure is plotted for the seven velocity configurations. It can be observed a well established and monotonic trend of noise gain, around ~6 dB at each increment of 20 km/h in the vehicle's velocity. Also, all the curves present quite similar shape in the whole frequency range 50-3000 Hz. Additionally, the acoustic radiated power computed as in integral of acoustic intensity at a semi-spherical surface is presented in figure 5b. Similar trends are observed as in figure 5a for all the velocity configurations, i.e. a noise gain ~6 dB at each increment of 20 km/h in the vehicle's velocity. In contrast, some of the
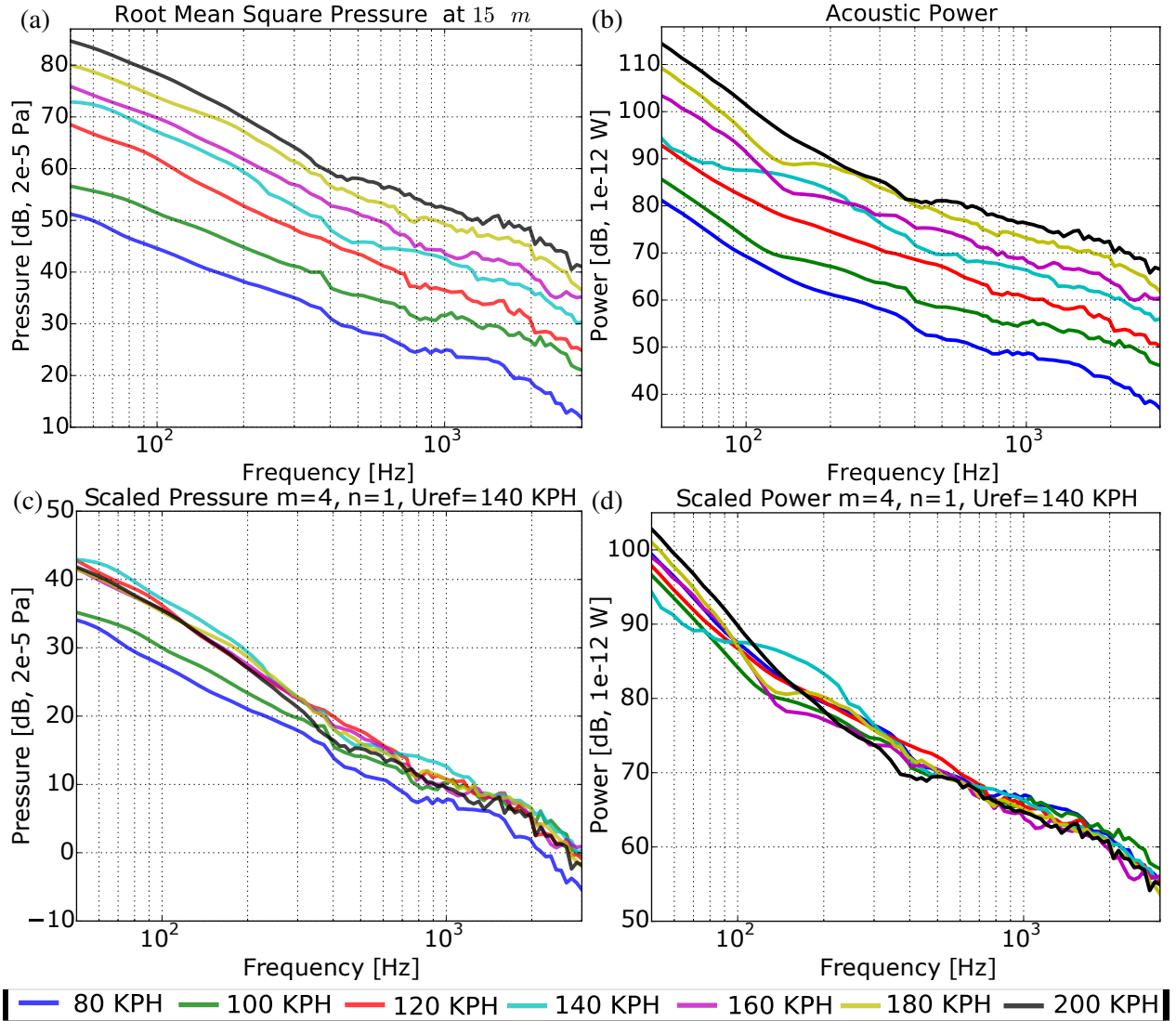
Fig. 5. – Integral values of acoustic field. (a) Root average square pressure computed at a semi sphere of 15 m of diameter for all the velocity configurations. (b) Acoustic radiated power computed at the same semi-sphere than figure (a). (c) Similar as (a) but all the curves scaled by a factor $(U/U_{ref})^{(n-m)/2}$ where $m = 4$ and $n = 1$. (d) Similar as (b) but all the curves scaled by a factor $(U/U_{ref})^{\alpha(m-n)/2}$ where $m = 4$, $n = 1$, $\alpha = 9$.

curves corresponding to lower vehicle's velocities (cyan - 140 km/h and yellow 180 km/h) cross curves with higher vehicle velocities (magenta - 160 km/h and black - 200 km/h), however, the behaviors of such curves are quite monotonic and smooth in contrast to the local pressure in the near field depicted in figures 4a-c.

The general behavior observed in figures 5a,b is a linear increase for the acoustic presure in dB as the vehicle's velocity increases. This may be interpreted as a power law for the frequency, pressure and power scaling with respect to the vehicle's velocity:[7]

$$f_{\text{scaled}} = f\left(\frac{U}{U_{\text{ref}}}\right)^{-n} , \quad p_{\text{scaled}} = p\left(\frac{U}{U_{\text{ref}}}\right)^{-(m-n)/2} , \quad W_{\text{scaled}} = W\left(\frac{U}{U_{\text{ref}}}\right)^{-\alpha(m-n)/2} , \quad (9\text{a-c})$$
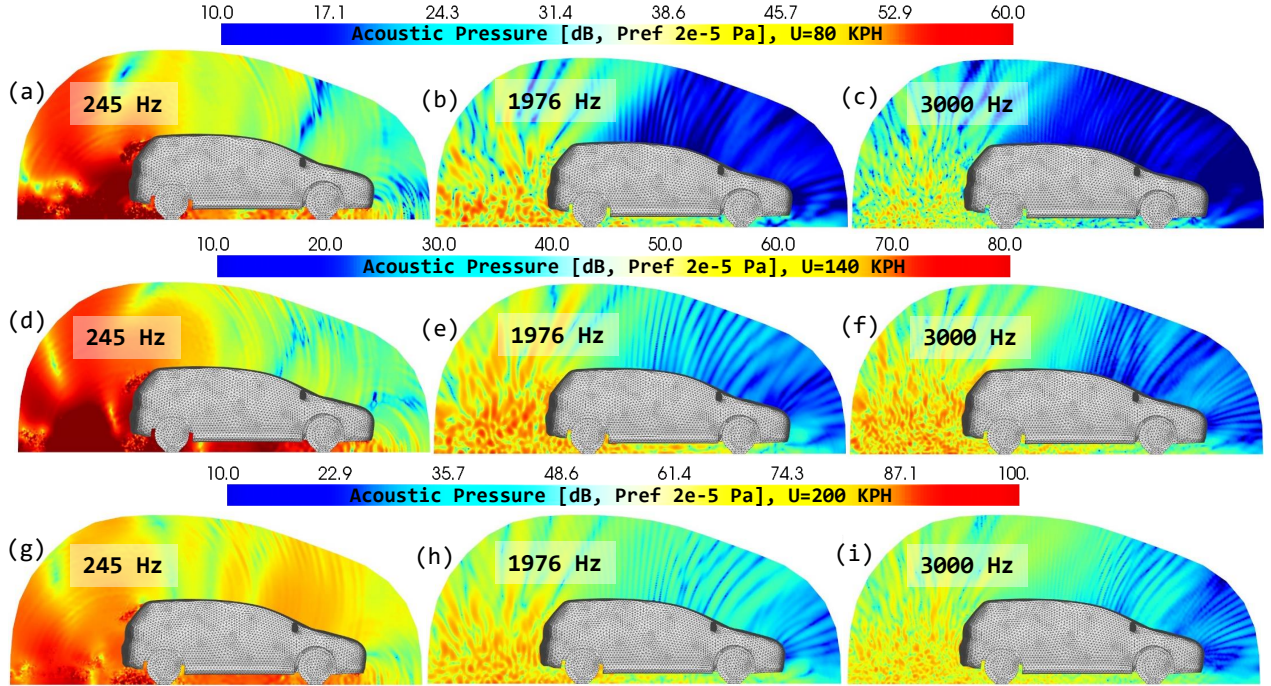
Fig. 6. – Maps for acoustic pressure in the near field in dB *($p_{ref} = 2 \times 10^{-5}$* Pa*). Three different velocities are shown, (a-c)* 80 km/h*, (d-f)* 140 km/h *and (g-i)* 200 km/h *for three different frequencies* 245 Hz*,* 1976Hz *and* 3000 Hz *indicated at each figure.*

where f is the frequency, U is the vehicle's velocity, U_{ref} is the reference velocity in this case is set to 140 km/h, W is the acoustic power and n, m and α are empirical constant to be fitted. It is well known that large turbulent structures induce a frequency shift in the pressure spectra as the velocity increases,[8] for instance, the Von Kármán vortex shedding frequency shifts to higher frequencies for larger flow velocities. These large turbulent structures are hardly predicted with SNGR method. On the other hand, fine scale turbulence's energy will shift upwards the pressure spectra as the velocity increases.[8] This kind of fine structures is well predicted with SNGR method. For instance, in figure 5c the scaled pressure spectra using equation (9b) is plotted with no frequency shift (9a) for $m = 4$ and $n = 1$ as in Hartmann et al.[7] All the curves collapse in a diagonal narrow band of ~ 7 dB of thickness with some separations at lower frequencies while better merging at higher. Furthermore, a similar scaling law (9c) is applied for the power spectra in figure 5d with no frequency shift (9a) for $m = 4$, $n = 1$ and a supplementary factor $\alpha = 9$. It can be observed how all the curves collapse better than in figure 5c, specially at higher frequencies while at lower some separation occurs.

A few maps illustrating the amplitude of the acoustic pressure are depicted in figures 6a-i and 7a-d. For instance, pressure patterns similarities are observed for the three frequencies 245 Hz (figures 6a,d,g), 1976 Hz (figures 6b,e,h) and 3000 Hz (figures 6c,f,i) as the vehicle's velocity increases. In general, high pressure patterns are observed at the rear of the vehicle with zones of silence predominantly present at the front for higher frequencies. Furthermore, the pressure patterns over the wall of the vehicle's body are plotted in figures 7a-d for four different frequencies 245, 725, 1976 and 3000 Hz at the velocity configuration 140 km/h. The acoustic pressure over the wall reveals extensive high pressure zones near the side-mirror and driver's window at low frequencies (245 and 725 Hz) while at higher, such high pressure zone are well confined at the vicinity of size-mirror.
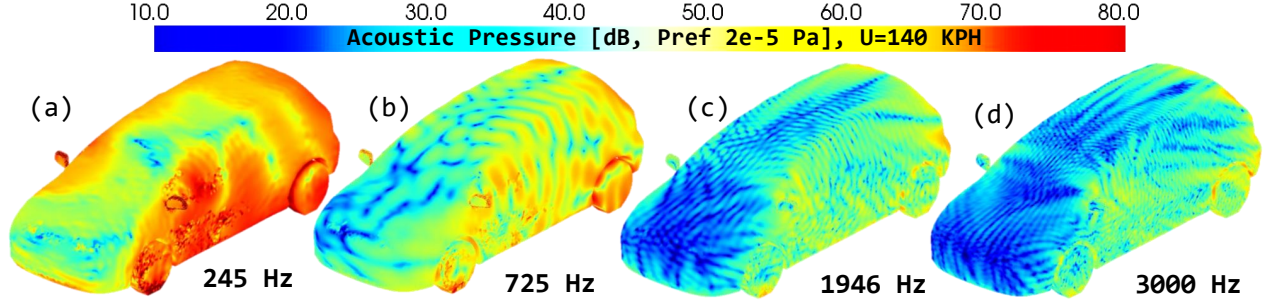
Fig. 7. – Map for acoustic pressure over the vehicle's surface for velocity 140 km/h with frequency indicated at each figure. Four frequencies are plotted 245, 725, 1946 and 3000 Hz.

Some comments about the computational time and memory consumption are finally addressed. The acoustic computations corresponding to the *ActranDGM* model were performed in 2 GPU accelerators *Nvidia Tesla K80* with 24 GB each (domain parallelism) taking in average 973 s (total time 7d21h11m for 700 cases, i.e. 7 velocities × 100 frequencies) with 6.2 Gb of memory consumption per case, i.e. a total of 378 GPU.h. Predictions of computational time has been made using other types of computer architectures by running 15% of the total simulations cases each time. First, the current implementation of SNGR sources in *ActranDGM* solver allows parallel computations in multiple CPUs using MPI communicators, for instance in cluster of 64 processors Intel (R) CPU E3-1240 V2 @ 3.40 GHz, the 15% of the total computations took 1d18h51m, extrapolating, the total computational cost would be 11d21h40m, i.e. a total of 18283 CPU.h. Secondly, the total computational time has been estimated by using 1 GPU accelerator *Nvidia Tesla P100* with 16 GB. For instance, the computational cost for the 15% of the total cases adds up to 1d7h11m using the *Nvidia Tesla P100* card, making an extrapolation, the total computational time (700 cases) would be 8d16h27m, i.e. a total of 208 GPU.h. Although, the GPU.h ratio between the *Nvidia Tesla P100* and *Nvidia Tesla K80* is around 1.81, the architecture corresponding to 2 GPU accelerators *Nvidia Tesla K80* have been chosen to perform all computational cases because: (i) slightly less computational times, around ∼ 1d of different; (ii) the combined memory available, i.e. 2 × 24 Gb (2 *Nvidia Tesla K80*) versus 16 Gb (*Nvidia Tesla P100*), needed to properly handle the aeroacoustic sources.

6 CONCLUDING REMARKS

An efficient method for the computation of aerodynamic sound based on high-order DG approach has been presented. The aerodynamic sources imposed at the right-hand side of the LEE are estimated from the synthetization of the turbulent velocity field represented as a finite sum of statistically independent random Fourier modes (SNGR). The sources are mapped inside the high-order acoustic elements to accurately represent the physical phenomena. The generation of the aerodynamic sources relies on the turbulence statistics from computationally inexpensive CFD solutions, i.e. RANS-CFD, which are a very common standard in industry. Also, the numerical method used for solving the acoustic propagation (DG) has high parallel scalability suited to large acoustic problems and high frequency. Subsequently, the results presented for the full car configuration at different speeds properly correlate with empirical scaling laws based on experimental data. This demonstrates the pertinence of the method for relative comparisons of various pre-designs/prototypes and further classification based of their acoustic performance.

In contrast to computational aeroacoustics approaches based on unsteady CFD solutions, e.g. LES, the method proposed in this work highly reduces the computational effort related to the CFD process. Furthermore, the method may be used to extend the frequency range of aeroacoustic simulations based on unsteady CFD solution beyond cut-off frequency related to the grid's size. Finally, future work includes the modelling of sound generated aerodynamically in large industrial context such as high-speed trains or aircraft applications.

REFERENCES

1. Tam, C. K. (1995). Computational aeroacoustics issues and methods. AIAA journal, 33(10), 1788-1796.
2. Bailly, C., & Juve, D. (1999). A stochastic approach to compute subsonic noise using linearized Euler's equations. In 5th AIAA/CEAS Aeroacoustics Conference and Exhibit (p. 1872).
3. Cabrol, M., Detandt, Y. & Talbot A. Efficient method for car exterior noise prediction based in steady cfd input. ICSV 24, London, United Kingdom , 23 to 27 July 2017. (2016)
4. Chevaugeon, N., et al. Efficient discontinuous Galerkin methods for solving acoustic problems. *In 11th AIAA/CEAS Aeroacoustics Conference* (p. 2823), (2005).
5. Legendre, C., et al. Towards large aeroacoustic applications through a hybrid approach based on the linearized Euler equations. ICSV 23, Athens, Greece 10 to 14 July 2016. (2016)
6. Free Field Technologies S.A. Actran 18.0 User's Manual, (2017).
7. Hartmann, M., et al. (2012). Wind Noise caused by the A-pillar and the Side Mirror flow of a Generic Vehicle Model. In 18th AIAA/CEAS Aeroacoustic Conference, AIAA paper (Vol. 2205, p. 2012).
8. Tsuji, Y., Fransson, et al. (2007). Pressure statistics and their scaling in high-Reynolds-number turbulent boundary layers. J. Fluid Mech., 585, 1-40.
9. Lighthill, M. J. On sound generated aerodynamically. I. General theory. *P. Roy. Soc. (London) A-Math. Ph.*, **211**(1107), 564-587, (1952).
10. Lighthill, M. J. On sound generated aerodynamically. II. Turbulence as a source of sound. *P. Roy. Soc. (London) A-Math. Ph.*, **222**(1148), 1-32, (1954).
11. Kraichnan, R. H. (1970). Diffusion by a random velocity field. The physics of fluids, 13(1), 22-31.
12. Karweit, M., et al. (1991). Simulation of the propagation of an acoustic wave through a turbulent velocity field: A study of phase variance. The Journal of the Acoustical Society of America, 89(1), 52-62.
13. Software Cradle Co., ScTetra Version 13, User's Guide, Basic of CFD Analysis. 2017.
14. Kato, M. and Launder, B. E. (1993), The Modeling of Turbulent Flow Around Stationary and Vibrating Square Cylinders, Proc. 9th Symposium on Turbulent Shear Flows, Kyoto, August 1993, pp. 10.4.1-10.4.6.